

Umbellate Distortions of the Uranyl Coordination Environment Result in a Stable and Porous Polycatenated Framework that can Effectively Remove Cesium from Aqueous Solutions

Yanlong Wang,^{1,2} Zhiyong Liu,^{1,2} Yuxiang Li,^{1,2} Zhuanling Bai,^{1,2} Wei Liu,^{1,2} Yaxing Wang,^{1,2} Xiaomei Xu,^{1,2} Chengliang Xiao,^{1,2} Daopeng Sheng,^{1,2} Juan Diwu,^{1,2,*} Jing Su,^{3,4,*} Zhifang Chai,^{1,2} Thomas E. Albrecht-Schmitt,⁵ and Shuao Wang^{1,2,*}

¹School for Radiological and Interdisciplinary Sciences (RAD-X), Soochow University, 199 Ren'ai Road, Suzhou 215123, China.

²Collaborative Innovation Center of Radiation Medicine of Jiangsu Higher Education Institutions, 199 Ren'ai Road, Suzhou 215123, China

³Shanghai Institute of Applied Physics and Key Laboratory of Nuclear Radiation and Nuclear Energy Technology, Chinese Academy of Sciences, Shanghai 201800, China

⁴Department of Chemistry & Key Laboratory of Organic Optoelectronics and Molecular Engineering of the Ministry of Education, Tsinghua University, Beijing 100084, China

⁵Department of Chemistry and Biochemistry, Florida State University, 95 Chieftain Way, Tallahassee, Florida 32306, United States

Contents

S1. Materials and instrumentations

S2. Synthetic methods

S3. X-ray crystallography

S4. Circular dichroism (CD) spectrum and Second Harmonic Generation (SHG) experiments

S5. Computational details

S6. Thermogravimetric analysis

S7. Surface area measurements

S8. pH-stability measurements

S9. β and γ radiation resistance measurements

S10. Cs^+ exchange experiments

S11. Spectroscopic characterizations

S1. Materials and instrumentations. All reagents and solvents were used as received from commercial suppliers without further purification. The infrared spectra of KBr pellets were recorded in the range of 4000-450 cm^{-1} on a Thermo Nicolet 6700 spectrometer. Elemental analyses (C, H, and N) were performed with a Vario EL CHNOS elemental analyzer. Powder X-ray diffraction (PXRD) data were collected from 3 to 50° with a step of 0.02° and the time for data collection was 0.5 s on a Bruker D8 Advance diffractometer with Cu K α radiation ($\lambda=1.54056$ Å) and a Lynxeye one-Dimensional detector. The experimental PXRD patterns of the two samples match well with the simulated ones, revealing that they are both single phase without any impurity (see figures in section S9 of β and γ radiation resistance measurements). Thermalgravimetric analysis was carried out on a NETZSCH STA 449F3 instrument in the range of 30-900 °C under a nitrogen flow at a heating rate of 10 °C/ min. The solid-state luminescence and UV-vis-NIR spectra were recorded on a Craic Technologies microspectrophotometer, crystals were placed on quartz slides under Krytox oil, and data was collected after optimization of microspectro-photometer. A Quantachrome Autosorb Gas Sorption analyzer IQ2 was used to perform N₂ adsorption measurements. Scanning electron microscopy/energy-dispersive spectroscopy (SEM/EDS) images and data were collected using FEI Quanta 200FEG. The energy of the electron beam was 30 kV, and the spectrum acquisition time was 100 s. Inductively coupled plasma mass spectrometry (ICP-MS) analysis of Cs was conducted using a Thermo Finnigan high resolution magnetic sector Element 2 ICP-MS instrument. Circular dichroism (CD) spectra were taken on a Jasco J-810 spectrodichromometer (sample was prepared as a solid pellet by mixing 1 mg sample of **1** with 100 mg KCl). Second Harmonic Generation (SHG) experiments were executed by Kurtz-Perry powder SHG test using an Nd:YAG laser (1064 nm) with input pulse of 350 mV. The values of the nonlinear optical coefficients for SHG have been determined by comparison with a KDP reference.

S2. Synthetic methods.

Synthesis of [(CH₃)₂NH₂][UO₂(L1)]·DMF·6.5H₂O (1**).** H₃L1 (43.8 mg, 0.1 mmol) and UO₂(NO₃)₃·6H₂O (50.2 mg, 0.1 mmol) were dissolved in 5 mL of DMF. Then 45 μL of concentrated nitric acid (65 wt%) were added to the mixtures, the resulting solution was sealed in a 20 mL glass vial and heated at 90 °C for 2 days. The reaction system was cooled slowly to

room temperature. After filtration and washing with DMF, ethanol, light yellow plate like crystals suitable for X-ray structural analysis were collected. **Yield:** ca. 59.3% (based on $\text{UO}_2(\text{NO}_3)_2 \cdot 6\text{H}_2\text{O}$). Anal. Calcd for $\text{C}_{32}\text{H}_{43}\text{O}_{15.5}\text{N}_2\text{U}$: C, 40.81; H, 4.60; N, 2.97 Found: C, 41.31; H, 2.99; N, 2.88.

Synthesis of $[(\text{CH}_3)_2\text{NH}_2][\text{UO}_2(\text{L2})] \cdot 0.5\text{DMF} \cdot 15\text{H}_2\text{O}$ (2). The preparation of compound **2** was similar to compound **1** except that 30 μL concentrated nitric acid were added. After filtration and washing with DMF, light yellow needle like crystals suitable for X-ray structural analysis were collected. **Yield:** ca. 40.8 % (based on $\text{UO}_2(\text{NO}_3)_2 \cdot 6\text{H}_2\text{O}$). Anal. Calcd for $\text{C}_{25}\text{H}_{52.5}\text{O}_{23.5}\text{N}_{1.5}\text{U}$: C, 29.78; H, 2.57; N, 1.97 Found: C, 29.96; H, 5.39; N, 2.14.

S3. X-ray crystallography. Data collection was performed on a Bruker D8-Venture diffractometer with a Turbo X-ray Source (Mo- $\text{K}\alpha$ radiation, $\lambda = 0.71073 \text{ \AA}$) adopting the direct-drive rotating anode technique and a CMOS detector at room temperature. The data frames were collected using the program APEX2 and processed using the program SAINT routine in APEX2. The structures were solved by direct methods and refined by the full-matrix least squares on F^2 using the SHELXTL-97 program.^[1] All non-hydrogen atoms were refined with anisotropic displacement parameters. Hydrogen atoms attached to carbon atoms were placed in geometrically idealized positions and included as riding atoms (C-H bond fixed at 0.97 \AA). Crystallographic and refinement details are summarized in Table S1. Selected bond lengths and angles for compound **1** and **2** are listed in Tables S2 and S3, respectively. For **1** and **2**, the solvent molecules in the structure are highly disordered and impossible to refine using conventional discrete-atom models. To resolve this issue, the contribution of solvent-electron density was removed using the SQUEEZE routine in PLATON^[2], thereby producing a set of solvent-free diffraction intensities. The final formulas were calculated from the SQUEEZE results in combination with those of elemental analyses and TGA.

Table S1. Crystallographic data for all of the compounds (after squeeze)

Sample	1	2
Formula	C ₂₇ H ₁₅ O ₈ U	C ₂₁ H ₁₁ O ₈ U
<i>Mr</i> [g mol ⁻¹]	705.42	629.33
Crystal system	Trigonal	Hexagonal
Space group	<i>P</i> 3 ₁ 21	<i>P</i> -62 <i>c</i>
<i>a</i> (Å)	17.3260(5)	18.4811(6)
<i>b</i> (Å)	17.3260(5)	18.4811(6)
<i>c</i> (Å)	39.892(2)	17.2261(13)
α	90.00	90.00
β	90.00	90.00
γ	120.00	120.00
<i>V</i> (Å ³)	10370.8(7)	5095.3(5)
<i>Z</i>	12	6
<i>D_c</i> (g cm ⁻³)	1.355	1.231
μ (mm ⁻¹)	4.730	4.805
<i>F</i> (000)	3996	1758
T(K)	273(2)	273(2)
GOF on <i>F</i> ²	0.855	0.811
R1, ^a wR2 ^b (<i>I</i> > 2σ(<i>I</i>))	0.0475, 0.1213	0.0587, 0.1230
R1, ^a wR2 ^b (all data)	0.0676, 0.1299	0.0909, 0.1370

$$^a R_1 = \sum(F_o - F_c)/\sum F_o; wR_2 = [\sum w(F_o^2 - F_c^2)^2/\sum w(F_o^2)^2]^{1/2}$$

Table S2. Selected bond lengths (Å) and angles (°) for compound **1**

Selected Bond Lengths (Å)			
U2-O6	1.776 (6)	U2-O2	1.773 (6)

U2-O12	2.448 (7)	U2-O4	2.457 (7)
U2-O8	2.446 (8)	U2-O15	2.492 (6)
U2-O9	2.477 (9)	U2-O16	2.482 (8)
U1-O1	1.754 (7)	U1-O3	1.769 (7)
U1-O5	2.482 (7)	U1-O10	2.423 (8)
U1-O11	2.459 (8)	U1-O7	2.441 (8)
U1-O13	2.478 (7)	U1-O14	2.483 (7)
Selected Bond Angles (°)			
O1-U1-O3	177.7 (3)	O1-U1-O5	94.1 (2)
O3-U1-O5	88.2 (3)	O1-U1-O10	92.9 (2)
O3-U1-O10	88.2 (3)	O1-U1-O11	87.6 (3)
O3-U1-O11	91.0 (3)	O1-U1-O13	91.0 (3)
O3-U1-O13	88.1 (3)	O1-U1-O14	90.2 (2)
O3-U1-O14	87.4 (3)	O1-U1-O7	89.1 (3)
O3-U2-O7	92.0 (3)	O6-U2-O2	178.9 (3)
O6-U2-O12	91.9 (3)	O2-U2-O12	88.2 (3)
O6-U2-O4	86.7 (3)	O2-U2-O4	94.2 (4)
O6-U2-O8	90.1 (3)	O2-U2-O8	89.1 (4)
O6-U2-O15	90.1 (3)	O2-U2-O15	89.0 (3)
O6-U2-O9	92.5 (3)	O2-U2-O9	87.2 (3)
O6-U2-O16	89.6 (3)	O2-U2-O16	91.4 (3)

Table S3. Selected bond lengths (Å) and angles (°) for compound **2**

Selected bond lengths (Å)			
U1-O4	1.728 (8)	U1-O5	1.805 (9)
U1-O1 ($\times 2$)	2.440 (7)	U1-O2 ($\times 2$)	2.426 (6)
U1-O3 ($\times 2$)	2.480 (7)		
Selected Bond Angles (°)			
O5-U1-O1	94.0 (3)	O4-U1-O1	85.3 (3)
O5-U1-O2	90.36 (16)	O4-U1-O2	89.59 (16)
O5-U1-O3	94.2 (3)	O4-U1-O3	86.5 (3)
O4-U1-O5	179.2 (5)		

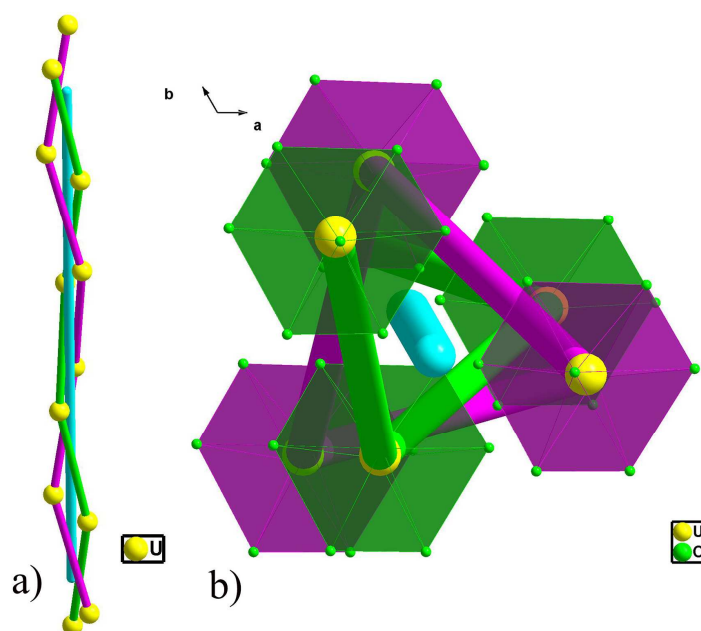


Figure S1. Depiction of chirality-originating 3_1 symmetry along c axis viewed from two different directions, each uranium atom is selected from different graphene-like layers. Uranium atoms are shown in yellow, oxygen atoms are shown in green, 3_1 screw axis are shown as light blue stick, and purple and green sticks represent two different sets of 3_1 symmetry-related uranium atoms.

S4. Circular dichroism (CD) spectrum and Second Harmonic Generation (SHG) experiments.

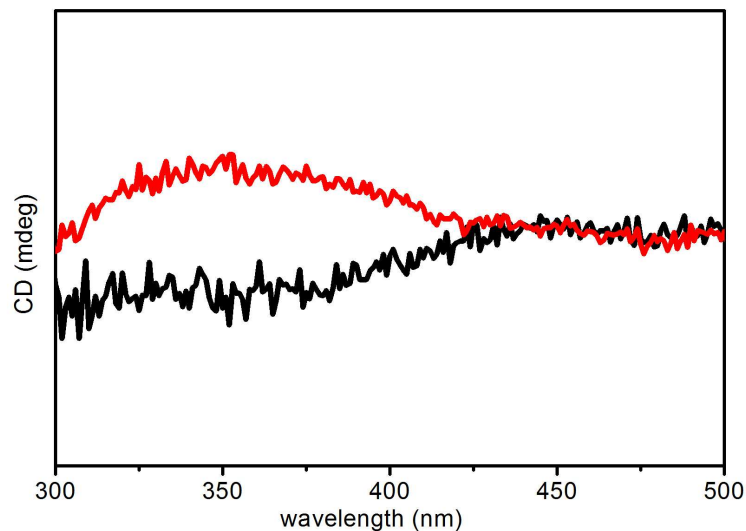


Figure S2. Circular dichroism (CD) spectra of **1**, where black and red lines represent two batches of spectra taken on randomly picked bulk crystals of **1**. The mirror image relation for the dichroic signal at ca. 350 nm can be assigned to two different enantiomorphs of **1**, clearly confirming its chiral nature and the presence of both enantiomorph crystals in the products.

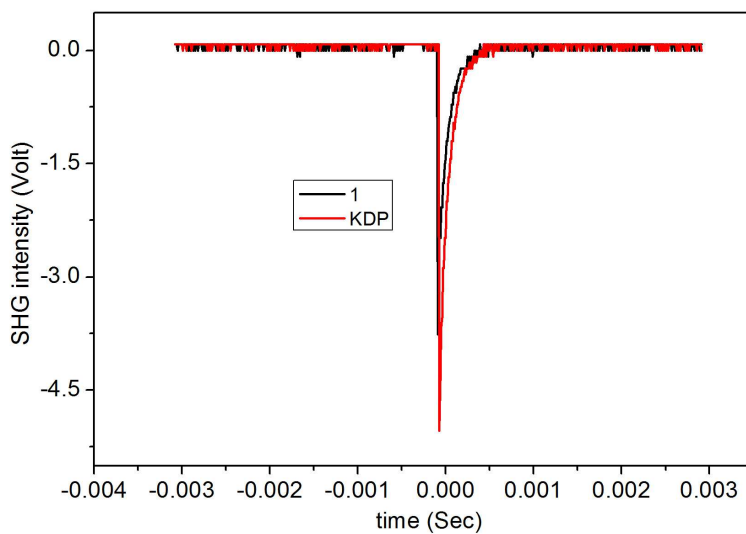


Figure S3. The SHG intensities of compound **1** ($0.8 \times \text{KDP}$) confirming its noncentrosymmetric nature.

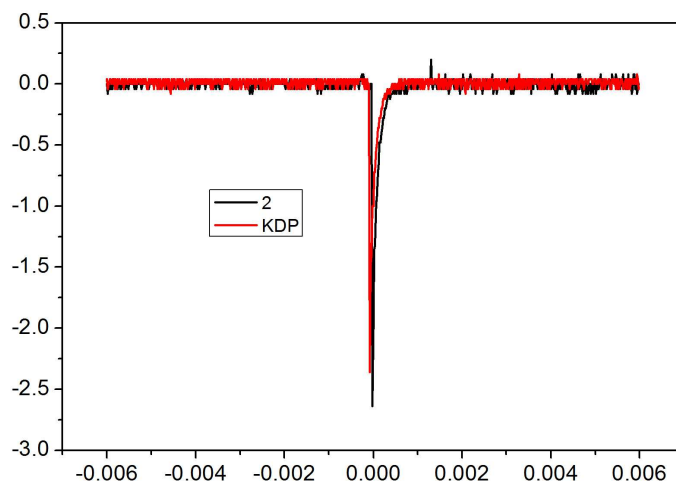


Figure S4. The SHG intensities of compound **2** ($1.1 \times \text{KDP}$) confirming its noncentrosymmetric nature.

S5. Computational Details. To understand the influence of equatorial distortion on the interaction between uranyl and polycarboxylate ligand in compound **2**, we performed linear transit (LT) calculations on two model compounds $[\text{UO}_2(\text{RCOO})_3]^-$ ($\text{R}=\text{H}, \text{Ph}$) by constrained optimizations at each LT coordinate along $\angle \text{O}_{\text{t1}}\text{UO}_{\text{c}}$ decreasing direction from 90° to 70° with a step of 2° , where O_{t1} means the terminal oxygen 1 of uranyl unit and O_{c} means the carboxyl atoms (see Figure 3 in the main text and Figure S5). The C_{3v} symmetry was used in the constrained optimizations except the starting point, i.e. $\angle \text{O}_{\text{t1}}\text{UO}_{\text{c}}=90^\circ$, corresponding to the ground-state $[\text{UO}_2(\text{RCOO})_3]^-$ ($\text{R}=\text{H}, \text{Ph}$) with D_{3h} symmetry instead. Further energy decomposition analyses (EDA) were performed at each LT geometry to evaluate the trends of total bonding energy and its components (i.e. steric and orbital interactions) for the two fragments, UO_2^{2+} and $(\text{RCOO})_3^{3-}$. These calculations were carried out by using the DFT/B3LYP method^[3] at the scalar relativistic (SR) level in Amsterdam Density Functional (ADF 2013.01) Program.^[4,5,6] The Slater basis sets with the quality of triple- ζ plus two polarization functions (TZ2P)^[7] were used, with the frozen core approximation applied to the inner shells $[1s^2-4f^{14}]$ for U and $[1s^2]$ for C and O. The scalar relativistic effects were taken into account by the zero-order regular approximation (ZORA).^[8]

When $\angle O_{t1}UO_c$ decreases from 90° to 70° , the $U\equiv O_{t1}$ bond length decreases by 0.04 \AA , and the $U\equiv O_{t2}$ bond length varies little with a slight increase of 0.01 \AA (see Figure 3 in the main text and Figure S5). It should be noted that the experimental value of the bond distance difference between $R(U\equiv O_{t1})$ and $R(U\equiv O_{t2})$ (0.077 \AA) is larger than the calculation value ($\sim 0.02 \text{ \AA}$), and that using a larger ligand $PhCOO^-$ to replace $HCOO^-$ does not improve this agreement, which is most likely due to the effects from the compact three-set polycatenation structure, and more specifically, the strong interactions between intercross layers marked in different colors in Figure 2(d) in the main text, which give rise to strong ligand fields imposing on one of the two terminal oxygen atoms, i.e., O_4 in Figure 1(d) in the main text. The distances between the terminal O_4 atom and the three nearest ligand hydrogen atoms in the intercross layer are 2.47 , 2.47 and 2.97 \AA , respectively, in the crystal compound 2, as shown in Figure S6.

When $\angle O_{t1}UO_c$ decreases, both of the Steric and Orbital interactions become relatively positive, as well as the resulting total bonding energy (see Figure S7, S8 and Table S4, S5). This bonding analysis result shows that both ionic and covalent interaction between uranyl and $RCOO^-$ ($R=H, Ph$) ligands are weakened as the ligand coordination gradually departing from the equatorial plane. The resulting instability is not significant, which is estimated as less than 16 kJ/mol in energy when $\angle O_{t1}UO_c$ is not lower than 84° . This small energy change will not strongly affect the stability of the crystal structure.

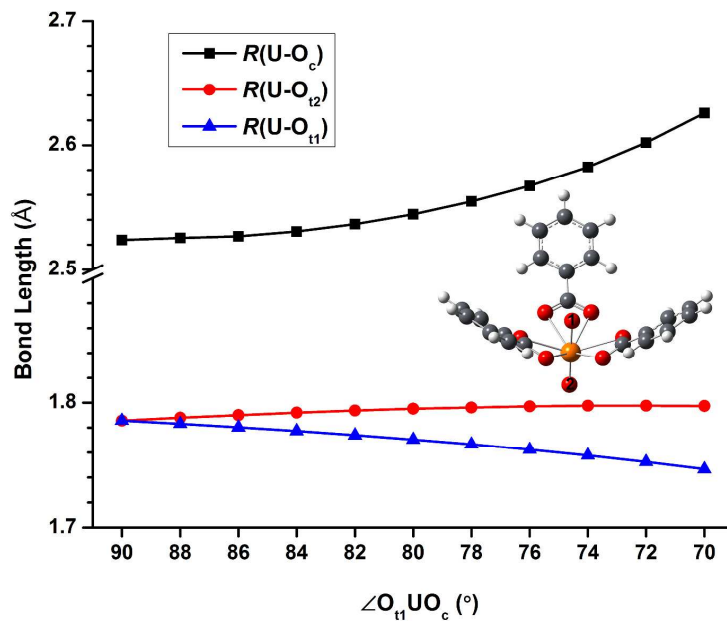


Figure S5. Trend of bond lengths between uranium and coordinated oxygen atoms in $[UO_2(PhCOO)_3]^-$ as the decrease of $\angle O_{t1}UO_c$: $R(U=O_{t1})$, $R(U=O_{t2})$ and $R(U-O_c)$, where O_t means terminal oxygen of uranyl unit, and O_c means carboxyl oxygen.

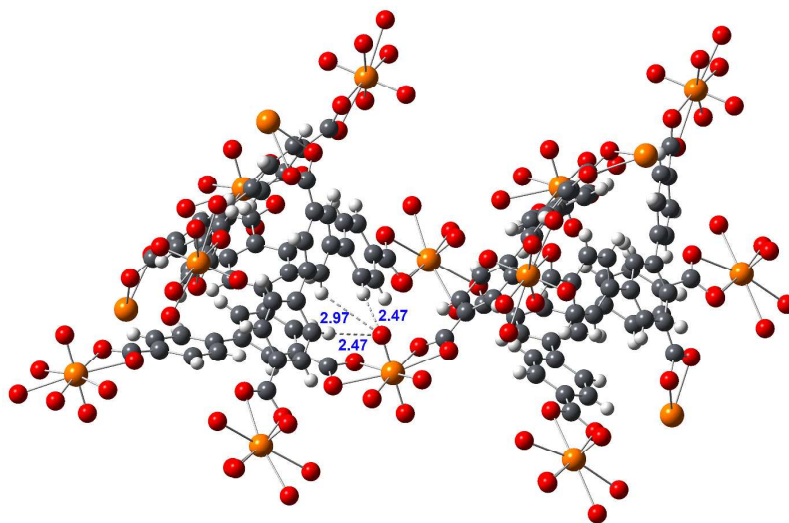


Figure S6. Packing view of 1 x 1 x 1 cell of crystal compound 2, and the distances between the terminal O_4 atom and the three nearest ligand hydrogen atoms in the intercross layer are 2.47, 2.47 and 2.97 Å, respectively.

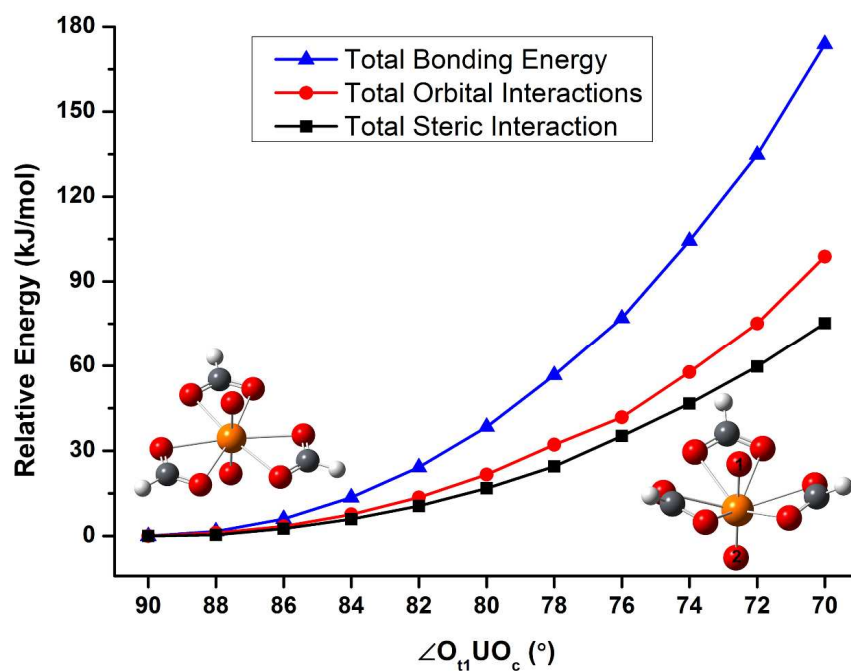


Figure S7. Linear transit (LT) energy curves illustrating transition from D_{3h} - $[UO_2(OOCH)_3]^-$ to C_{3v} - $[UO_2(OOCH)_3]^-$ along $\angle O_{t1}UO_c$ decreasing from 90° to 70° with a step of 2° . Energies are obtained from SR-DFT/B3LYP constraint optimization calculations at each fixed $\angle O_{t1}UO_c$. The starting point with $\angle O_{t1}UO_c = 90^\circ$ corresponds to the D_{3h} structure and the ending point with $\angle O_{t1}UO_c = 70^\circ$ corresponds to the C_{3v} structure in the figure.

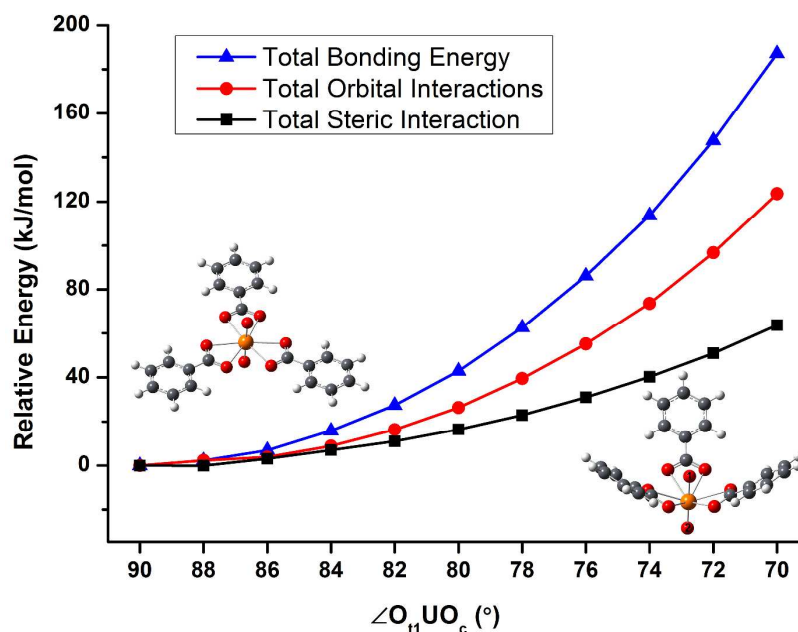


Figure S8. Linear transit (LT) energy curves illustrating transition from D_{3h} - $[UO_2(OOCPh)_3]^-$ to C_{3v} - $[UO_2(OOCPh)_3]^-$ along $\angle O_{t1} UO_c$ decreasing from 90° to 70° with a step of 2° . Energies are obtained from SR-DFT/B3LYP constraint optimization calculations at each fixed $\angle O_{t1} UO_c$. The starting point with $\angle O_{t1} UO_c = 90^\circ$ corresponds to the D_{3h} structure and the ending point with $\angle O_{t1} UO_c = 70^\circ$ corresponds to the C_{3v} structure in the figure.

Table S4. Energy decomposition analysis (EDA) results in kJ/mol at each geometry of LT energy curves for $[UO_2(HCOO)_3]^-$

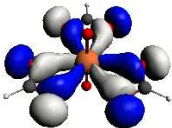
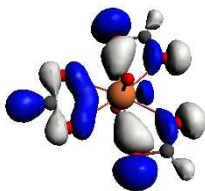
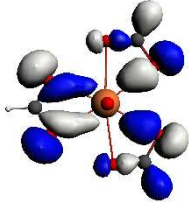
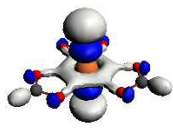
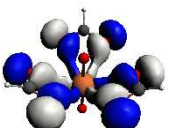
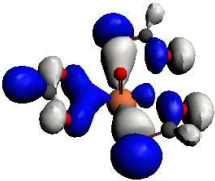
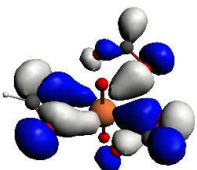
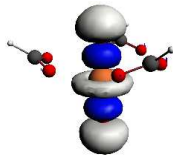
LT#	$\angle O_{t1} UO_c$	Pauli Repulsion	Electrostatic Interaction	Total Steric Interaction	Total Orbital Interactions	Total Bonding Energy
0	90°	0.0 (783.9)	0.0 (-3479.2)	0.0 (-2695.3)	0.0 (-947.9)	0.0 (-3643.2)
1	88°	-1.4	1.8	0.5	1.2	1.7
2	86°	-3.4	6.0	2.6	3.4	6.0
3	84°	-7.3	13.3	6.0	7.6	13.6
4	82°	-13.2	23.8	10.6	13.6	24.2

5	80°	-20.6	37.4	16.8	21.7	38.4
6	78°	-30.2	54.6	24.5	32.2	56.7
7	76°	-35.5	70.6	35.2	41.8	77.0
8	74°	-49.4	96.0	46.6	57.8	104.4
9	72°	-67.7	127.4	59.7	75.1	134.8
10	70°	-89.8	164.9	75.1	98.8	173.9

Table S5. Energy decomposition analysis (EDA) results in kJ/mol at each geometry of LT energy curves for $[\text{UO}_2(\text{PhCOO})_3]^-$

LT#	$\angle \text{O}_{\text{tl}}\text{UO}_c$	Pauli Repulsion	Electrostatic Interaction	Total Steric Interaction	Total Orbital Interactions	Total Bonding Energy
0	90°	0.0 (770.2)	0.0 (-3182.3)	0.0 (-2412.1)	0.0 (-1070.0)	0.0 (-3482.1)
1	88°	-3.2	3.2	0.0	2.3	2.3
2	86°	-3.5	6.6	3.1	3.9	7.0
3	84°	-7.8	14.8	7.0	8.9	15.9
4	82°	-13.8	24.9	11.1	16.4	27.5
5	80°	-21.6	38.1	16.5	26.4	42.9
6	78°	-31.7	54.7	23.0	39.5	62.6
7	76°	-42.7	73.7	31.0	55.2	86.2
8	74°	-55.2	95.4	40.2	73.6	113.8
9	72°	-72.6	123.5	50.9	96.8	147.7
10	70°	-92.8	156.5	63.6	123.6	187.2

Table S6. The comparisons of corresponding orbitals between planar and distorted structure in equatorial plane (LT0 vs LT10) for $[\text{UO}_2(\text{HCOO})_3]^-$

LT#	$\angle \text{O}_{\text{t1}}\text{UO}_\text{c}$	$3a_2$	$13e-1$	$13e-2$	$12a_1$
0	90°				
10	70°				

S6. Thermogravimetric analysis. The as-synthesized dried samples were heated at a constant rate 10 K/min in nitrogen from 30°C to 900°C. Three weight loss steps are observed in compound **1**. The first 12.4 % (cal. 12.4 %) weight loss is attributed to the loss of free waters. The second is 7.6 % (cal. 7.8 %), which is attributed to the loss of free DMF. The last one is 5.0 % (cal. 4.9 %), which is attributed to the loss of protonated dimethylamine. Only one weight loss step is observed in compound **2** (found. 34.5 %, cal. 34.7 %), which can be attributed to the lost of free water, DMF and protonated dimethylamine cation.

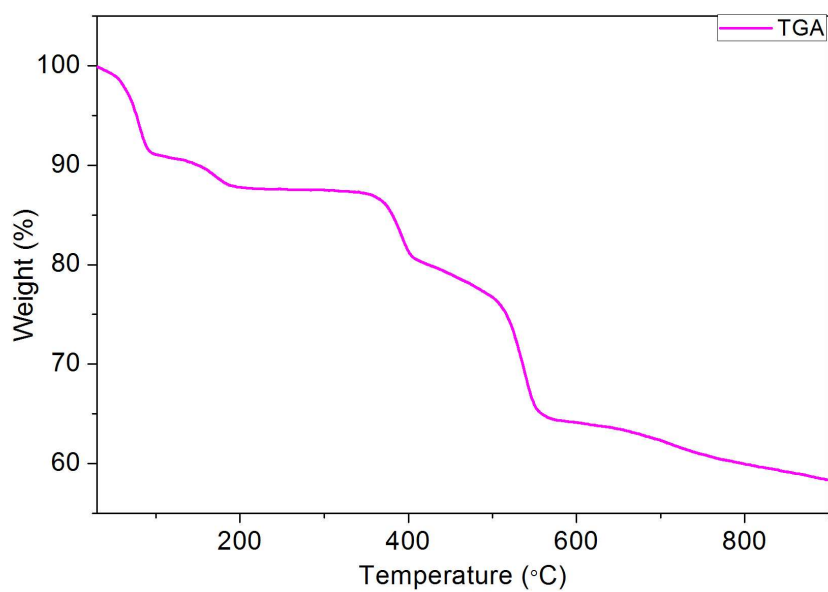


Figure S9. The TGA curve for compound 1

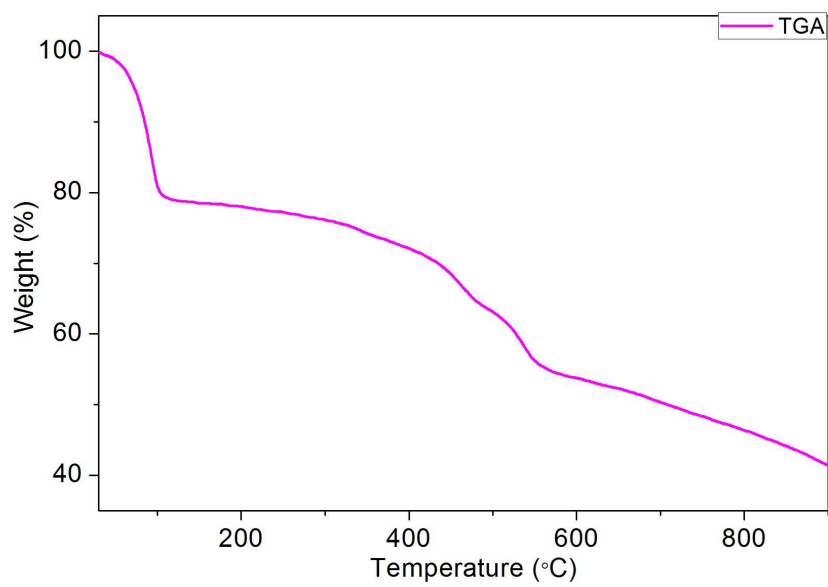


Figure S10. The TGA curve for compound 2

S7. Surface area measurements. Volumetric gas adsorption measurements for compound **2** were measured at 77 K with a liquid nitrogen bath, the detecting pressures range from 0 to 760 Torr respectively. All the measurements were conducted in the presence of high-purity gases. Methanol solution of LiNO₃ was added to the samples each 8 h and the extract was discarded, the sample was soaked for 3d to remove the solvent molecules. Similarly, the sample was further treated with methanol to remove the excess LiNO₃ in the solvent (soaked in methanol for 3d and fresh methanol was added every 8 h). After decanting the methanol extract, the sample was dried under a dynamic vacuum ($<10^{-3}$ Torr) at room temperature overnight. Before adsorption measurement, the sample was activated using the “outgas” function of the surface area analyzer for 10 h at 80°C.

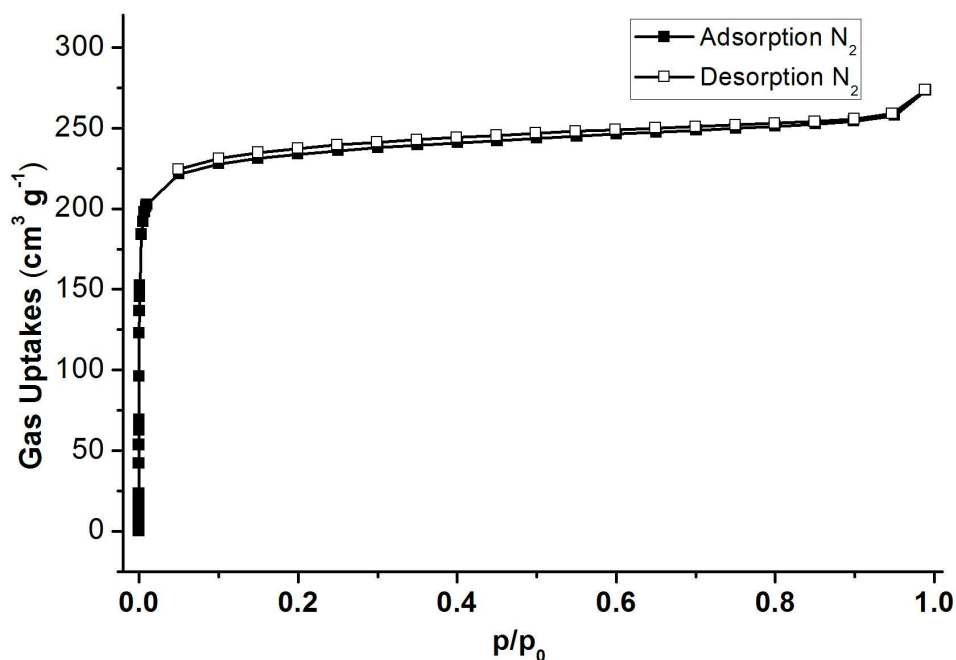


Figure S11. The N₂ adsorption and desorption isotherms for compound **2** at 77 K

S8. pH-stability Measurements. Water-stability measurements for compound **2** was studied by soaking the samples in HNO₃ or NaOH of different pH and shaken vigorously in an oscillator for

three days. The PXRD results demonstrate that **2** is stable in aqueous solutions within pH range from 3 to 12.

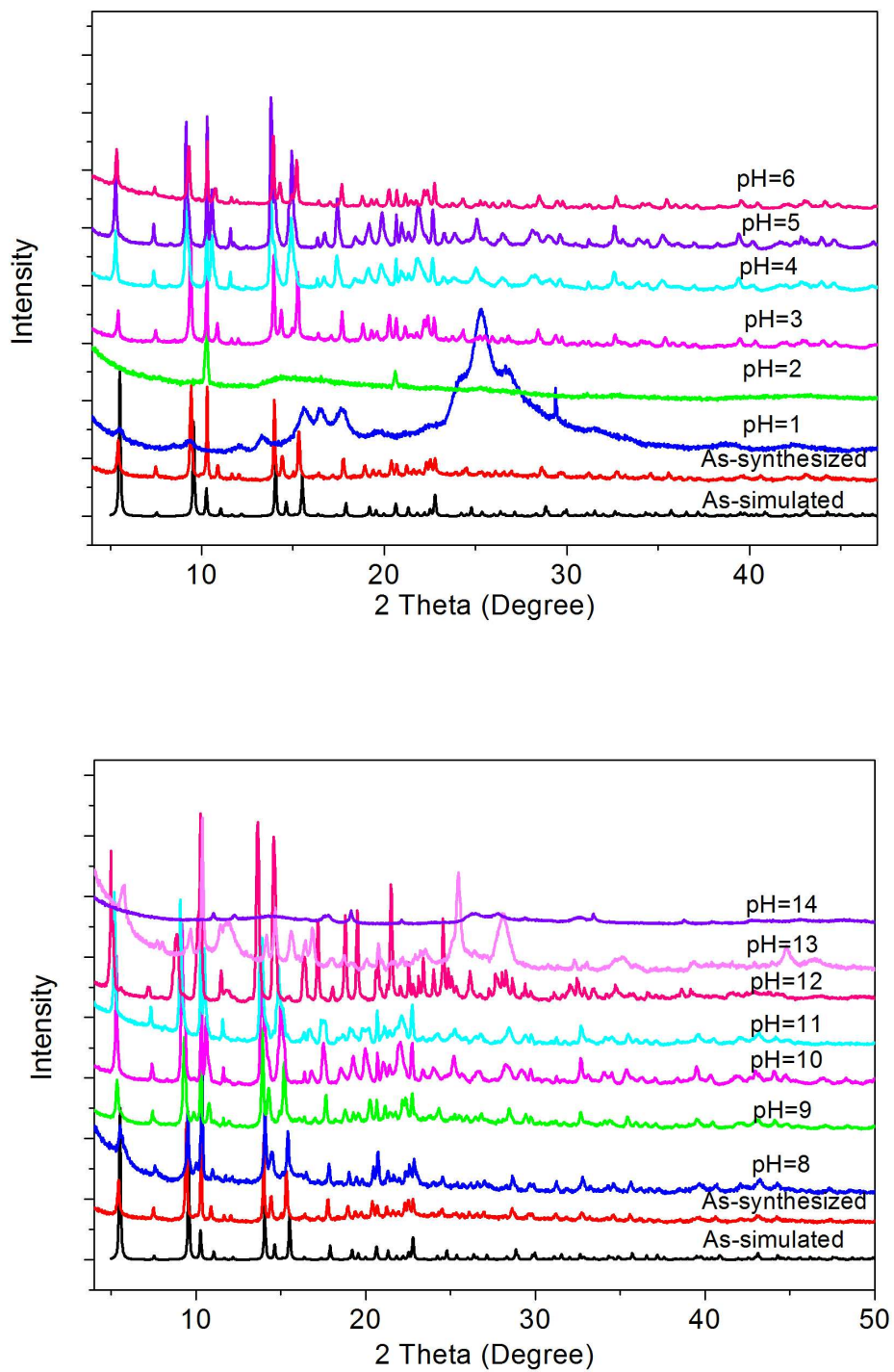


Figure S12. The PXRD for compound **2** after soaked in aqueous solutions at different pHs

S9. β and γ radiation resistance measurements. β irradiation experiment was conducted using electron beams (1.2 MeV) provided by an electron accelerator. Compounds **1** and **2** were irradiated at a dose rate of 20 kGy/hour for three different doses respectively: 10, 50, and 200 kGy. γ irradiation experiment was conducted using a ^{60}Co irradiation source (60000 curie). Compounds **1** and **2** were irradiated at a dose rate of 1.2 kGy/hour for five different doses respectively: 20, 80, 120, 160, and 200 kGy. The PXRD patterns for the irradiated samples match well with the originated samples and the simulated ones, which further confirm the excellent radiation resistance of the two samples.

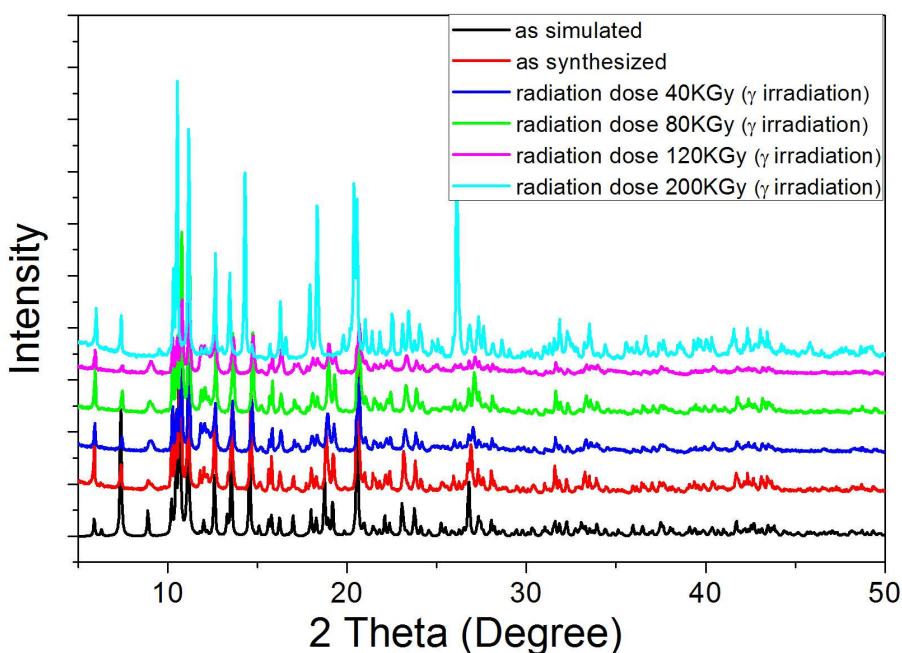


Figure S13. The powder X-ray diffraction (PXRD) patterns for compound **1** at different γ radiation dose.

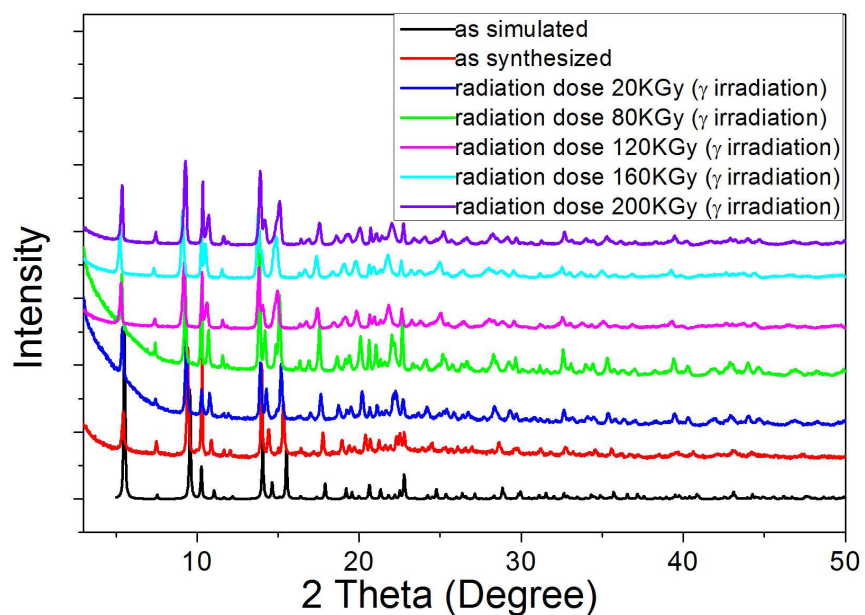


Figure S14. The powder X-ray diffraction (PXRD) patterns for compound **2** at different γ radiation dose.

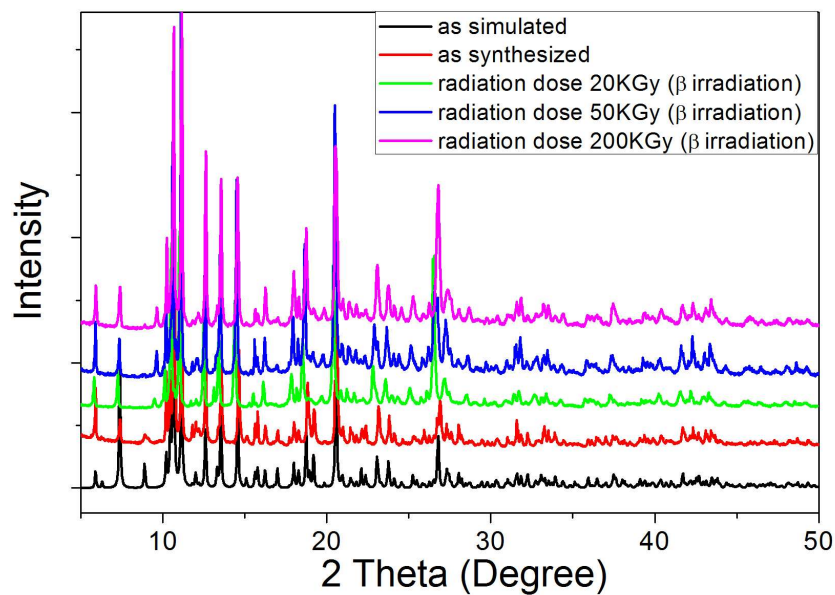


Figure S15. The powder X-ray diffraction (PXRD) patterns for compound **1** at different β radiation dose.

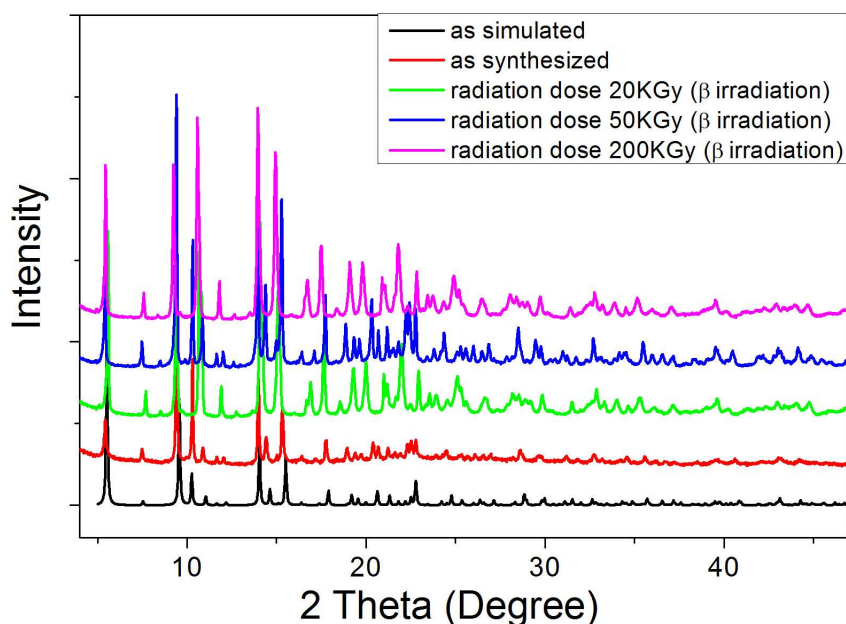


Figure S16. The powder X-ray diffraction (PXRD) patterns for compound **2** at different β radiation dose.

S10. Cs^+ exchange experiments. Cs^+ exchange measurements of compound **2** were studied by soaking 10 mg or 50 mg of compound **2** in 10 mL of water solutions of CsCl (1-500 ppm) with V/m ratio of either 200 or 1000 mL/g shown in the following result table (V is the volume of solutions and m is the mass of the adsorbent), the mixture was put on a shaker for a desired contacting time, and the ICP-MS measurements were used to detect the concentration of both initial and final Cs^+ solutions. The distribution coefficient K_d was calculated using the equation of $K_d = (V[(C_0 - C_e)/C_e])/(m)$, where C_0 and C_e are the initial and equilibrium concentration of Cs^+ .

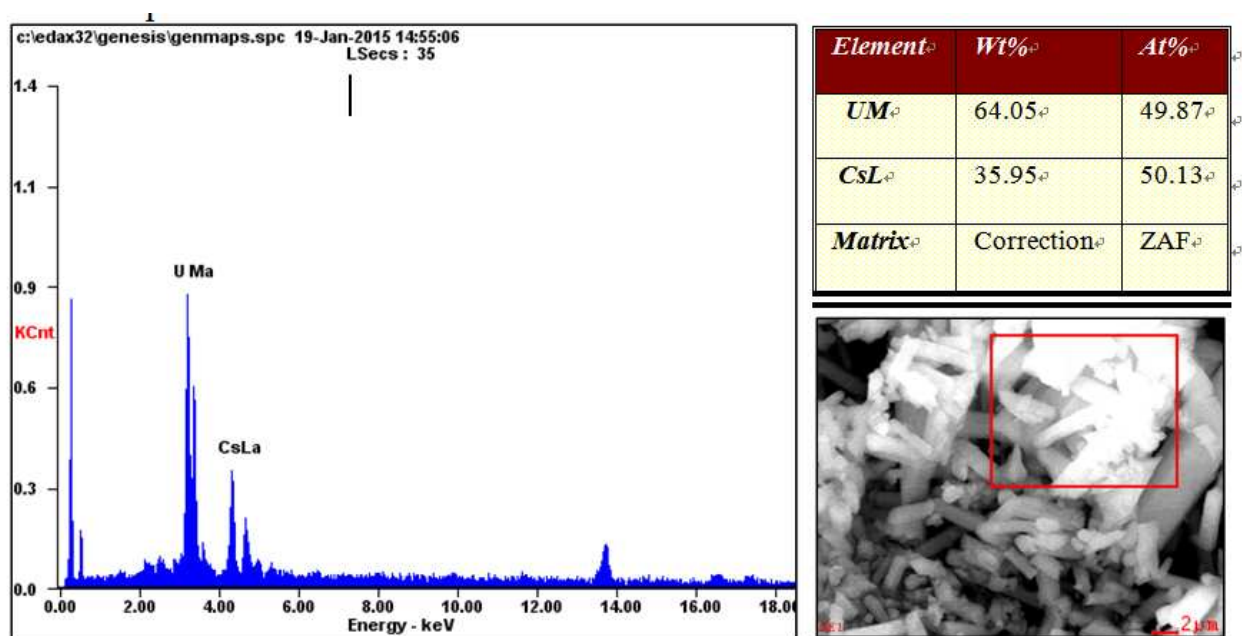


Figure S17. The EDS results for crystals of compound **2** soaked in solutions of Cs^+ (500 ppm) for 2 days.

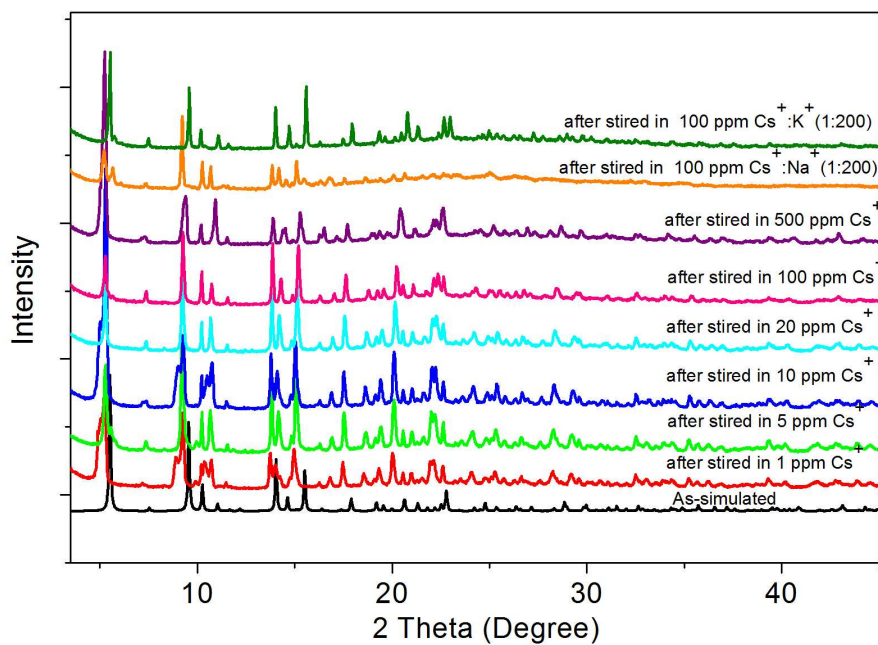


Figure S18. The PXRD for compound **2** after soaked in different solutions of Cs^+ for 2 days.

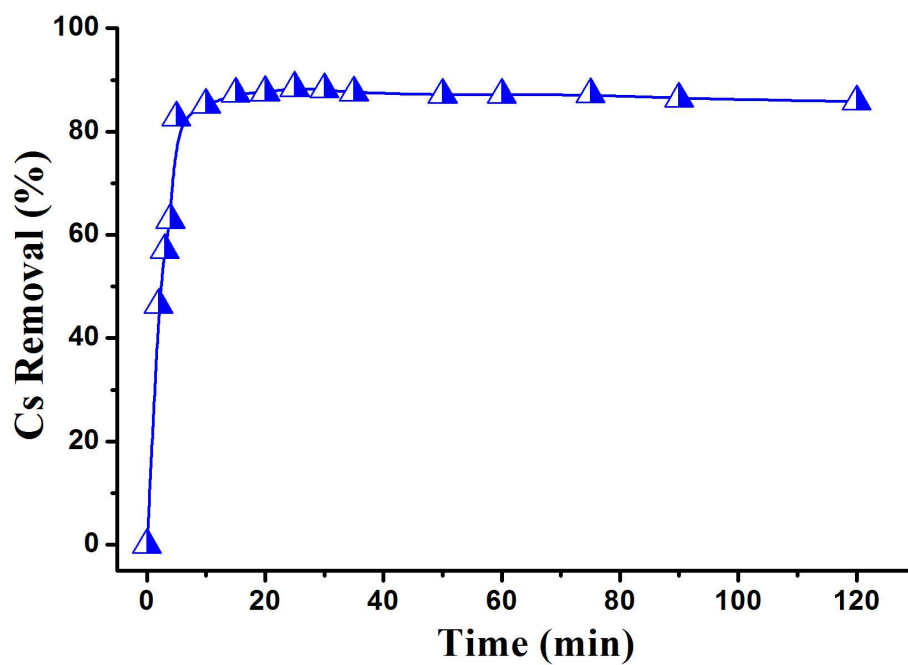


Figure S19. Cs⁺ exchange kinetics curves for the reaction containing 10 mL aqueous solution of 1 ppm Cs⁺ and 10 mg of **2**.

Table S7. Cs⁺ exchange measurements using compound **2**

Initial Cs concentration (ppm)	0.98	0.94	4.74	9.36	19.87	103.83	481.46
V/m(mL/g)	200 ^a	1000	1000	1000	1000	1000	1000
Final concentration (ppm)	0.05	0.11	1.01	2.59	5.76	47.92	336.25
%Cs Removal	94.51	88.30	78.69	72.33	71.01	53.85	30.16
K _d (Cs mL/g)	3443	7545	3693	2614	2450	1167	432

All of the Cs⁺ exchange reaction systems contain 10 mL aqueous solution and 10 mg of **2** except for ^a (50 mg of **2**).

Table S8. Cs⁺ exchange selectivity measurements using compound **2** (V/m = 200 mL/g)

Initial Cs concentration (ppm)	0.98	0.91	0.94	0.98	0.94	0.85	0.90
Competing cation	Cs	Li/Cs	Na/Cs	K/Cs	Rb/Cs	Mg/Cs	Ca/Cs
Mass ratio		5/1	5/1	5/1	5/1	5/1	5/1
V/m (mL/g)	200	200	200	200	200	200	200
Final concentration (ppm)	0.05	0.10	0.08	0.07	0.08	0.10	0.091
%Cs Removal	94.51	88.84	91.58	93.50	91.78	88.10	89.93
K _d (Cs mL/g)	3443	1592	2176	2877	2232	1480	1786
Initial Cs concentration (ppm)	0.98	0.79	0.96	0.98	0.92	0.84	0.92
Competing cation	Cs	Li/Cs	Na/Cs	K/Cs	Rb/Cs	Mg/Cs	Ca/Cs
Mass ratio		20/1	20/1	20/1	20/1	20/1	20/1
V/m (mL/g)	200	200	200	200	200	200	200
Final concentration (ppm)	0.05	0.20	0.14	0.12	0.09	0.24	0.21
%Cs Removal	94.51	74.21	85.88	87.81	88.70	71.81	77.71
K _d (Cs mL/g)	3443	576	1217	1440	1570	509	697

All of the Cs⁺ exchange reaction systems contain 10 mL aqueous solution and 50 mg of **2**.

Table S9. Cs⁺ exchange selectivity measurements using compound **2** (V/m = 1000 mL/g)

Initial Cs concentration (ppm)	0.94	0.91	0.94	0.98	0.94	0.85	0.90
Competing cation	Cs	Li/Cs	Na/Cs	K/Cs	Rb/Cs	Mg/Cs	Ca/Cs
Mass ratio		5/1	5/1	5/1	5/1	5/1	5/1
V/m (mL/g)	1000	1000	1000	1000	1000	1000	1000
Final concentration (ppm)	0.11	0.16	0.19	0.16	0.16	0.33	0.25
%Cs Removal	88.30	82.42	80.20	83.18	83.44	60.83	71.80
K _d (Cs mL/g)	7545	4690	4051	4943	5038	1553	2546

All of the Cs⁺ exchange reaction systems contain 10 mL aqueous solution and 10 mg of **2**.

Table S10. Cs⁺ exchange measurements at different pH using compound **2** (V/m = 1000 mL/g)

Initial Cs concentration (ppm)	0.92	1.03	0.95
pH	pH = 3	pH = 4	pH = 6
V/m (mL/g)	1000	1000	1000
Final concentration (ppm)	0.54	0.29	0.14
%Cs Removal	41.37	72.10	85.32
K _d (Cs mL/g)	706	2584	5811

All of the Cs⁺ exchange reaction systems contain 10 mL aqueous solution and 10 mg of **2**.

S11. Spectroscopic characterizations.

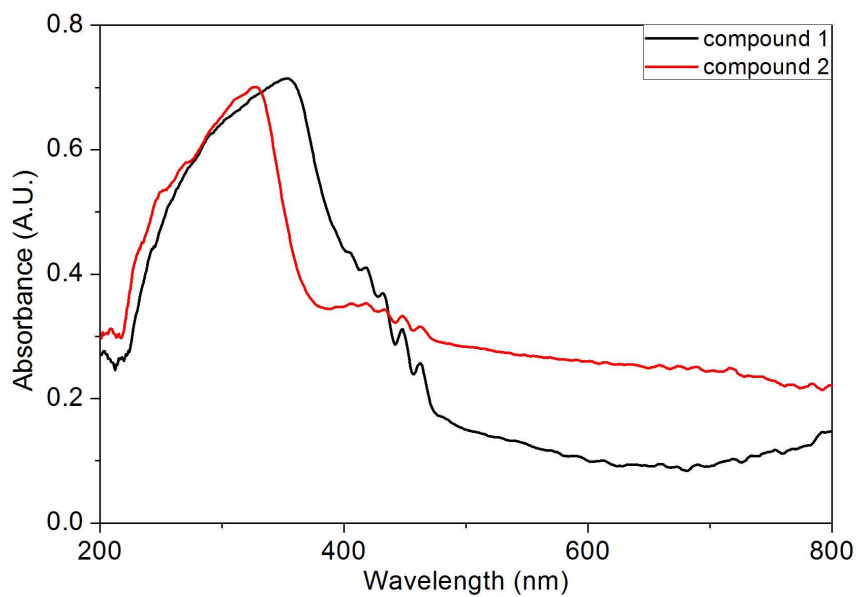


Figure S20. The UV-Vis absorption spectra for compound **1** and **2** measured at 298 K.

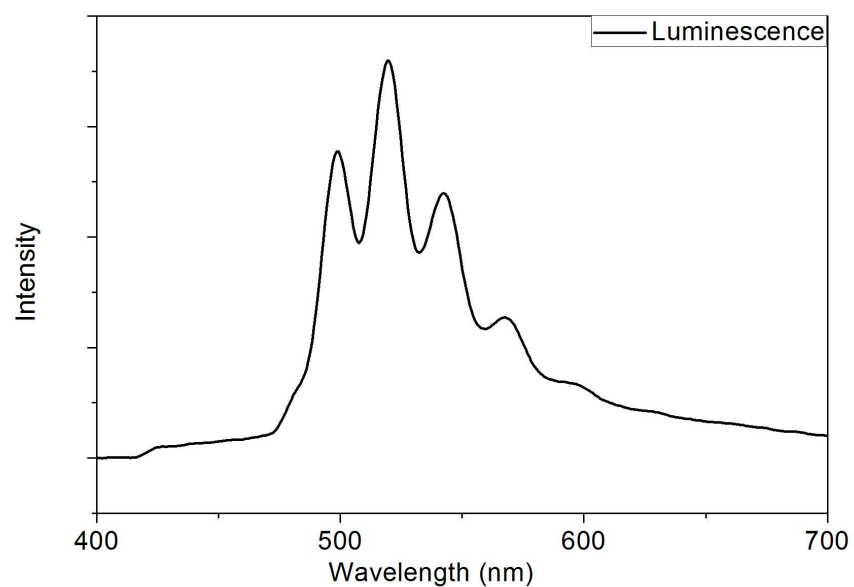


Figure S21. The emission spectrum for compound **2** measured at 100 K under excitation at 365 nm's light.

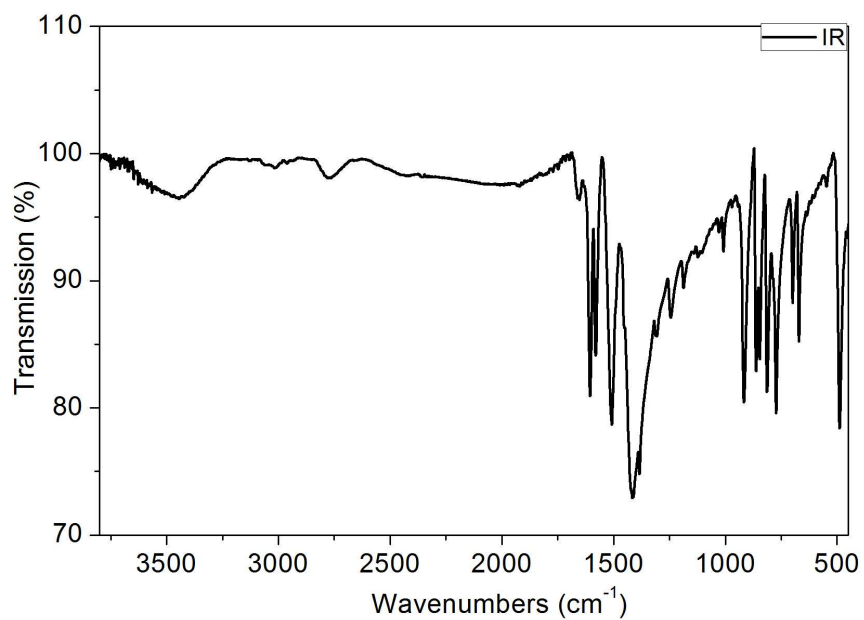


Figure S22. The IR spectrum for compound **1** measured at 298 K.

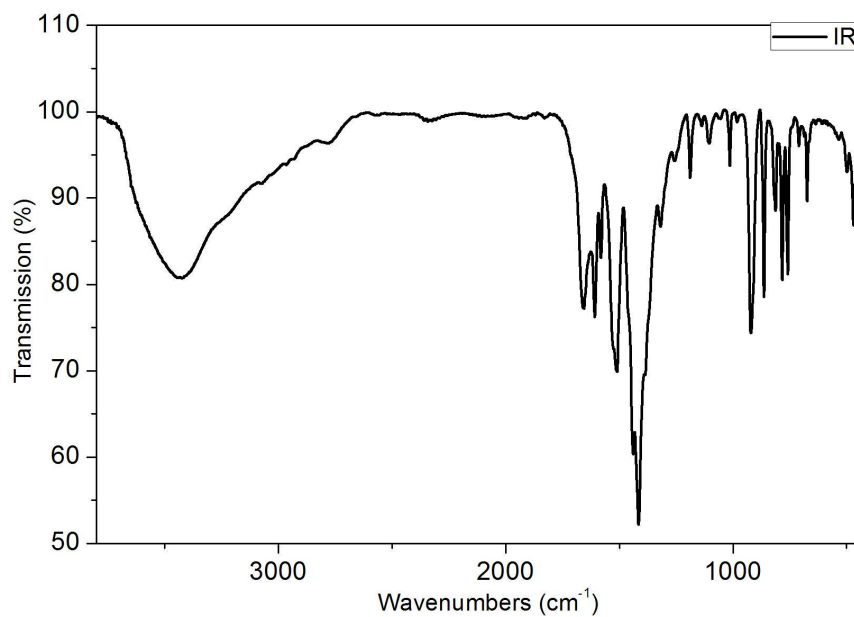


Figure S23. The IR spectrum for compound **2** measured at 298 K.

Reference:

- [1] SHELXTL, version 5.10; Siemens Analytical X-ray Instruments Inc.: Madison, WI, 1994.
- [2] O. Hübner, A. Glöss, M. Fichtner, W. Klopper, *J. Phys. Chem. A* **2004**, *108*, 3019-3023.
- [3] a) A. D. Becke, *Phys. Rev. A* **1988**, *38*, 3098–3100; b) C. Lee, W. Yang, R. G. Parr, *Phys. Rev. B* **1988**, *37*, 785-789.
- [4] ADF 2013.01, <http://www.scm.com>
- [5] C. Fonseca Guerra, J. G. Snijders, G. te Velde, E. J. Baerends, *Theor. Chem. Acc.* **1998**, *99*, 391-403.
- [6] G. te Velde, F. M. Bickelhaupt, E. J. Baerends, C. Fonseca Guerra, S. J. A. van Gisbergen, J. G. Snijders, T. Ziegler, *J. Comp. Chem.* **2001**, *22*, 931-967.
- [7] E. van Lenthe, E. J. Baerends, *J. Comp. Chem.* **2003**, *24*, 1142-1156.
- [8] E. van Lenthe, E. J. Baerends, J. G. Snijders, *J. Chem. Phys.* **1993**, *99*, 4597-4610.